Low-density ablator response to induction plasmatron aerothermal environments

Sreevishnu Oruganti[a,1], Lorenzo Capponi[a,1], Benjamin M. Ringel[a,1], Trey Oldham[a,1], Marco Panesi[a,1], Gregory S. Elliott[a,1], Sergio Fraile Izquierdo[c], Nagi N. Mansour[a,1], Francesco Panerai[a,1]

[a] *Department of Aerospace, University of Illinois at Urbana-Champaign, 104 S Wright St., Urbana, 61801, IL, US*
[b] *Center for Hypersonics and Entry Systems Studies, 1206 W Green St., Urbana, 61801, IL, US*
[c] *AMA Inc. at NASA Ames Research Center, Moffett Field, 94035, CA, US*

Contents

S1. Freestream Species Composition

Species composition of the freestream flow was computed using PlasFlowSolver [1], an ICP stagnation line code, with inputs of experimentally measured cold-wall heat flux, stagnation pressure and static pressure. Table S1 presents the species composition of the freestream flow for all the tested conditions. For the nitrogen tests, the flow is primarily composed of molecular nitrogen with the amount of atomic nitrogen increasing with torch power and stagnation pressure. Variations in mole fractions at the same condition between FF and PICA can be observed due to slightly lower mass flow rates used for the PICA tests.

For the air tests, the mole fraction of molecular oxygen is similar in order of magnitude to that of atomic oxygen for condition 1A, with approximately 6.3% of the flow being molecular oxygen and 15.3% being atomic oxygen. On the other hand, for conditions 2A-4A, the mole fraction of molecular oxygen is nearly negligible, causing atomic oxygen to be more prevalent. NO mole fraction is an order of magnitude higher for conditions 1A and 4A due to either lower torch power (condition 1A) or higher chamber pressure (condition 4A).

Table S1: Freestream species mole fractions along stagnation line for all the test conditions, estimated using PlasFlowSolver [1].

Condition	Sample ID	Material	X_{N_2}	X_N	X_{O_2}	X_O	X_{NO}
Nitrogen Plasma Tests							
1N	S1	FF	0.935	0.065	-	-	-
2N	S2	FF	0.701	0.299	-	-	-
3N	S3	FF	0.877	0.123	-	-	-
4N	S4	FF	0.853	0.147	-	-	-
3N	P1	PICA	0.876	0.124	-	-	-
1N	P12	PICA	0.968	0.032	-	-	-
2N	P13	PICA	0.765	0.234	-	-	-
3N	P11	PICA	0.864	0.136	-	-	-
Air Plasma Tests							
1A	S13	FF	0.755	0.000	0.066	0.153	0.026
2A	S12	FF	0.669	0.097	0.000	0.231	0.003
3A	S10	FF	0.743	0.022	0.000	0.230	0.006
4A	S11	FF	0.757	0.003	0.004	0.222	0.015
1A	P7	PICA	0.755	0.000	0.063	0.156	0.026
2A	P9	PICA	0.701	0.065	0.000	0.231	0.003
3A	P14	PICA	0.748	0.016	0.000	0.229	0.006
4A	P10	PICA	0.755	0.007	0.001	0.226	0.011

S2. Optical Emission Spectroscopy

S2.1. Nitrogen Plasma

Freestream OES measurements of the plasma jet are shown in Fig. S1. Since the mass flow rate between the FiberForm (FF) experiments and the PICA experiments were slightly different, OES for both test series showed variations in spectra. Spectral features were labeled with corresponding atomic and molecular transitions based on the NIST atomic spectra database and from literature [2, 3].

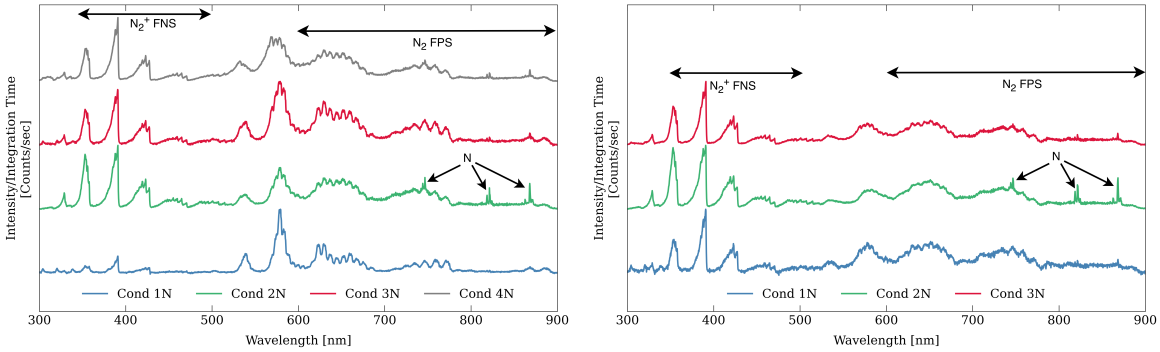

(a) Freestream OES for FF tests.

(b) Freestream OES for PICA tests.

Figure S1: Freestream OES of nitrogen plasma for FF and PICA tests.

For the FF runs, freestream spectra show a strong signal of the first positive system (FPS) of N_2 and first negative system (FNS) of N_2^+. At the lowest RF power and static pressure (condition 1N), atomic nitrogen signal is negligible indicating a predominantly molecular nitrogen plasma, and most of the emission signal is attributed to the N_2 FPS bands. As the RF power is increased, atomic nitrogen peaks are observed at 745, 821 and 869 nm for condition 2N. With increasing pressure at similar RF power (comparing conditions 3N and 4N), atomic nitrogen signal emission increased slightly, due to increased collisions at the higher pressure, causing N_2 to dissociate [4].

Freestream spectra for the PICA tests show similar trends of N_2 FPS and ${N_2}^+$ FNS, with increasing atomic nitrogen with power and pressure. However, as the mass flow rate for the PICA runs was slightly lower, a higher RF power had to be used, causing the ${N_2}^+$ FNS signal to be higher than the N_2 FPS signal. Additionally, the presence of atomic nitrogen is more pronounced for condition 2N than for the other two conditions.

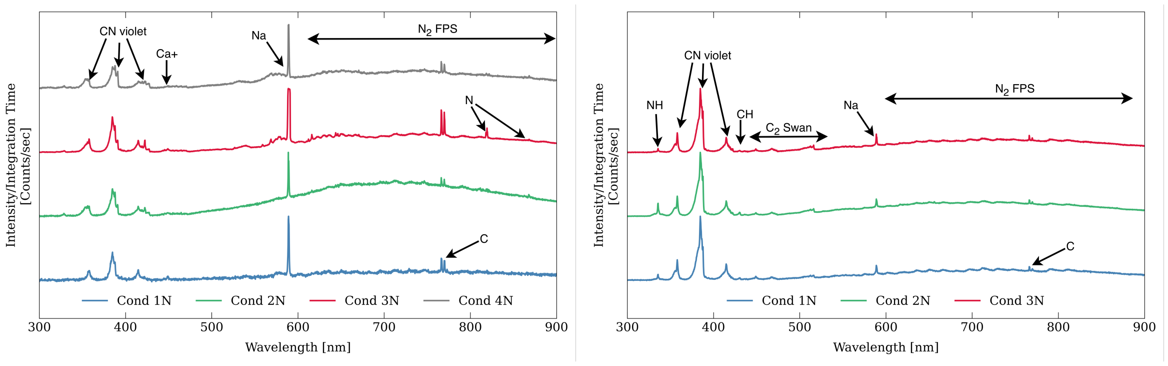

(a) FF.

(b) PICA.

Figure S2: OES of plasma ahead of stagnation point for (a) FF and (b) PICA after 10 seconds of insertion.

Fig. S2 shows the OES spectra at the same location after 10 seconds of sample insertion. For FF (in Fig. S2a), CN-violet emission is observed for all the conditions, indicating reactions of the nitrogen plasma with the carbon fibers. A prominent sodium signal is observed, which is a common contaminant in FF and is a highly radiating element. Signs of Ca^+ emission are observed which are also due to contaminants in FF [3]. Sputtered or sublimated carbon causes a doublet carbon peak centered around 767 nm to appear. Finally, a lower extent of atomic nitrogen signal is seen due to reaction with the carbon-fibers forming CN [3, 5–7] and due to overlapping Planck radiation from the sample surface.

In the PICA tests, peaks from resin pyrolyzing and reacting with the plasma cause NH and CH emission [3, 8] due to devolatilization of organic compounds at lower temperatures [9]. The signal of NH and CH (relative to that of CN-violet) increases with heat flux and is relatively similar at a higher pressure. The presence of C_2-swan has also been commonly observed for pyrolyzing phenolic resins and has been attributed to the decomposition of methylene bridges during pyrolysis [10, 11].

S2.2. Air Plasma

OES measurements of the freestream plasma were taken with an exposure time of 200 ms, and are shown in Fig. S3. Similar to the nitrogen plasma tests, emission signal from N_2 FPS and ${N_2}^+$ FNS is observed in all the cases for the air plasma tests. With increasing RF power or static pressure, the signal of ${N_2}^+$ FNS increases relative to that of N_2 FPS, along with increase in atomic nitrogen signal. Atomic oxygen signal is also observed in all the tests, with peaks at 777.2 nm and 844.6 nm. The intensity of the O-atom peaks also increases with increase in RF power or chamber pressure.

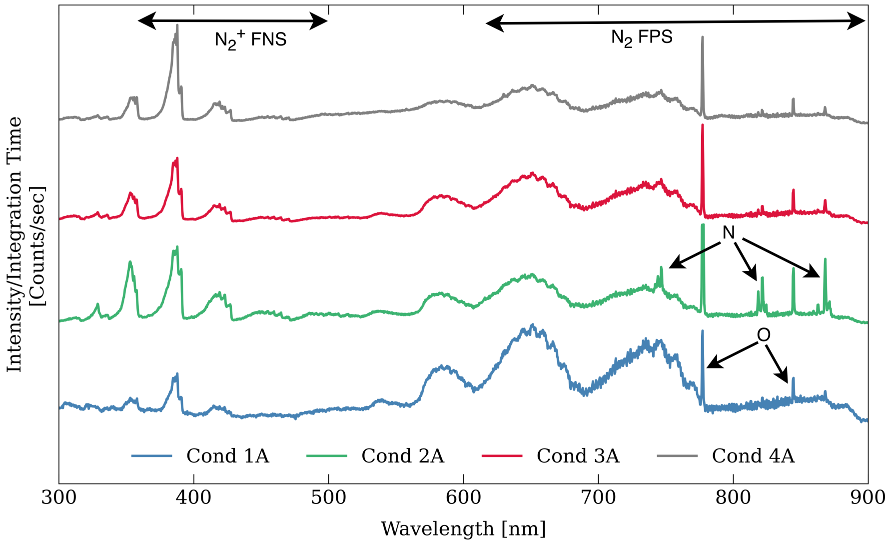

Figure S3: Freestream OES for air plasma at the different test conditions.

OES spectra of FF and PICA after 10 seconds of insertion into the plasma are shown in Fig. S4. For FF for conditions 2A and 4A, the signal was saturated due to using a high exposure time of 50 ms, after which it was reduced to 7.5 ms for the other tests. FF tests show peaks similar to those seen in the N_2 tests, with CN-violet and sodium being the dominant emitted species. In condition 3A, atomic nitrogen and oxygen are visible, indicating possibly augmented heating on the surface due to surface recombination. For the PICA tests, in addition to CN-violet and sodium, peaks from NH, CH and OH are observed. In particular, OH signal appears which is not seen in the N_2 plasma tests for PICA.

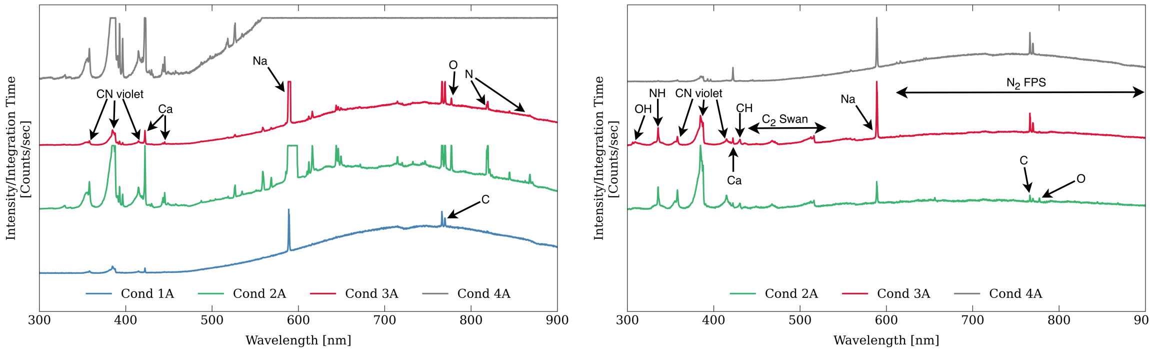

(a) FF.

(b) PICA.

Figure S4: OES of plasma ahead of stagnation point for (a) FF and (b) PICA after 10 seconds of insertion.

S3. Cross-Section Images of PICA

S3.1. Nitrogen Plasma

Post-test PICA samples were sectioned to characterize the extent of pyrolysis as a function of heat flux and pressure. Cross-sections of the samples are shown in Fig. S5.

(a) Condition 1N, sample P12 (low heat flux).

(b) Condition 3N, sample P11 (medium heat flux).

(c) Condition 2N, sample P13 (high heat flux).

Figure S5: Cross-sections of PICA samples tested in N_2 plasma.

From the cross-section images, virgin (non-pyrolyzed) and charred regions are clearly distinguishable in the three samples. The cross-sections show that the extent of pyrolysis increases with the heat flux of tests. Sample P12 (condition 1N) is pyrolyzed the least and shows the regions seen in a typical ablative material, namely virgin, pyrolysis and char zones. In sample P11 (condition 3N), a smaller virgin zone is visible with a larger portion of the sample being charred. At the highest heat flux tested (condition 2N), sample P13 is seen to be fully charred, with a possible indication of a thin pyrolysis zone near the bottom of the sample.

In samples P12 and P11 where the pyrolysis front is clearly visible, it can observed that the extent of pyrolysis is highest below the stagnation surface, followed by side-heating of the sample causing pyrolysis to occur from the sides. Similar side-heating was observed by Milos and Chen [12] and is non-negligible for modeling iso-Q material response.

S3.2. Air Plasma

Post-test PICA samples were sectioned to observe the extent of pyrolysis as a function of heat flux and pressure. Cross-sections of samples are shown in Fig. S6.

(a) Condition 1A, sample P7 (low heat flux).

(b) Condition 3A, sample P14 (medium heat flux).

(c) Condition 4A, sample P10 (medium heat flux).

(d) Condition 2A, sample P9 (high heat flux).

Figure S6: Cross-sections of PICA samples tested in air plasma.

From the cross-section images of post-test samples, the virgin, pyrolysis and char regions of the samples can be identified. Compared to the N_2 post-test cross-sections, the extent of pyrolysis is seen to be higher for conditions 1 and 3 in the air tests. In the air tests, with increasing heat flux, the extent of pyrolysis is seen to increase (comparing samples P7 and P9). Similar extents of pyrolysis for samples P14 and P10 are observed qualitatively when tested at similar heat fluxes but different pressures.

S3.3. Estimation of Pyrolysis Mass Loss

From the cross-section images of PICA, mass loss due to pyrolysis was estimated following the methodology proposed by Ringel et al. [13], and is detailed below. The image is first thresholded to obtain a mask that distinguishes the virgin region from the charred and partially pyrolyzed regions. A value of zero is assigned to the pixels that are in the fully charred region, and a value of unity is assigned to the pixels in the virgin region. For pixels that have colors between the virgin and char values, a linear gradient is mapped to account for regions containing partially charred phenolic. From the 2-dimensional mask, the fraction of the mask containing resin (f_r) is computed. Volume of the mask (V_{mask}) is estimated by revolving the 2-dimensional mask about the center of the sample, assuming that the samples pyrolyze in an axi-symmetric manner. The post-test mass of resin in the masked volume was then calculated as:

$$m_{res,f} = f_r \rho_{res} V_{mask} \tag{1}$$

Here, ρ_{res} is the density of the resin phase and is the difference of PICA and FF densities. PICA density (ρ_{PICA}) was calculated using the initial mass and volume of each virgin sample, and an average FF density ($\rho_{\bar{FF}}$) was calculated using the average mass of all the FF samples tested (= 163.5 kg/m^3). Additionally, the mass of the resin ($m_{res,0}$) in a virgin PICA sample can be calculated as the difference of the mass of the PICA sample and the average mass of the FF samples. From the initial and final resin mass, the mass loss due to pyrolysis was computed as:

$$\Delta m_{pyro} = (m_{res,0} - m_{res,f})(1 - \chi) \tag{2}$$

Here χ is the char yield of the phenolic resin in PICA, estimated to lie between 48% and 54%, and vary with heating rates as suggested by Guiles et al. [14]. Hence, for this study, a nominal value of 51% with ± 3% uncertainty was used for χ. From total mass loss of PICA samples, the mass loss due to recession in air plasma can then be obtained by subtracting the pyrolysis mass loss assuming negligible in-depth oxidation. Additionally, from the post-test sample mass (m_f), volume (V_f), resin mass ($m_{res,f}$), and volume of unpyrolyzed resin ($V_{res,f}$), the density of the charred PICA can be estimated neglecting in-depth oxidation, as:

$$\rho_{char} = \frac{m_f - m_{res,f} - \bar{\rho}_{FF} * V_{res,f}}{V_f - V_{res,f}} \tag{3}$$

Table S2 summarizes the contributions of pyrolysis and recession to mass loss along with char density of the PICA samples. From the char density of each PICA sample and the volume computed as a function of test time from the test video, the mass loss only due to recession of charred PICA while exposed to air plasma was estimated, and is presented in Fig. 18b of the main paper.

S4. Thiele Number Definition and Assumptions

The Thiele number is defined as [15]:

$$\Phi = \frac{L}{\sqrt{\frac{D_{eff}}{s_f k_f}}} \tag{4}$$

where L is a characteristic length of the sample, taken as the diameter (40 mm); s_f is the specific surface area of FiberForm (FF), computed from micro-CT as 54,223 m^2/m^3 [16]; and k_f is the fiber reactivity, modeled using Arrhenius kinetics.

Table S2: Estimates of mass loss due to pyrolysis and surface recession, along with char density

Sample ID	Δm_{pyro} [g]	$\Delta m_{recession}$ [g]	$\frac{\Delta m_{pyro}}{\Delta m_{tot}}$ [%]	Char density [g/cm^3]
P12	1.311 ± 0.080	0	95.93 ± 5.87	0.2267
P13	1.621 ± 0.010	0	98.52 ± 6.03	0.2168
P11	1.473 ± 0.091	0	97.43 ± 5.96	0.2139
P7	1.417 ± 0.087	0.379 ± 0.087	78.91 ± 4.83	0.2327
P9	1.56 ± 0.0955	1.073 ± 0.0955	59.25 ± 3.63	0.2274
P14	1.627 ± 0.10	0.401 ± 0.10	80.20 ± 4.91	0.2344
P10	1.605 ± 0.098	0.1062 ± 0.098	93.79 ± 5.74	0.2466

Atomic oxygen is highly reactive and primarily drives surface reactions, whereas molecular oxygen—though less reactive—can penetrate deeper into the porous structure due to similar diffusivity [17]. Therefore, the rate-limiting step for in-depth oxidation is assumed to be the reaction of molecular oxygen with carbon fibers:

$$\mathrm{C\,(s)} + \frac{1}{2}\,\mathrm{O_2} \longrightarrow \mathrm{CO} \tag{5}$$

with the rate given by the Park Arrhenius model [18]:

$$k_{f,\mathrm{O_2}}^{CO} = 100 \exp\left(\frac{-1.2 \times 10^5}{R_u T}\right) \tag{6}$$

The effective diffusivity D_{eff} is expressed as:

$$D_{eff} = \frac{\varepsilon}{\eta} D_{ref}, \tag{7}$$

where:

- **Porosity (ε):** For FF, ε is assumed to be 0.90 [6, 18].
- **Reference Diffusivity (D_{ref}):** Taken as the mixture-averaged diffusion coefficient of O_2 in air computed using Mutation++ [19] using local temperature and pressure.
- **Tortuosity (η):** Approximated using the Bosanquet relation [20]:

  $$\eta = \frac{\eta_b + \eta_{Kn} \cdot Kn}{1 + Kn} \tag{8}$$

  with $\{\eta_b, \eta_{Kn}\}$ from [18] as {1.1, 1.95} for through-thickness and {1.06, 1.64} for in-plane directions.

  Here, the Knudsen number is:

  $$Kn = \frac{\bar{\lambda}}{d_p} = \frac{1}{d_p} \cdot \frac{9.5 \times 10^{-8} \cdot 10^5 T}{298 p} \tag{9}$$

  where d_p is the pore size, taken as 50 μm for FF [6, 18]. Thus, some parameters depend only on temperature (e.g., fiber reactivity), while others depend on both temperature and pressure (e.g., Kn, η, D_{ref}).

S4.1. Flow-Field Simulations for Thiele Number Estimation

To obtain the stagnation pressure profile along the iso-Q surface, simulations of the Plasmatron X flow field were performed using the multi-physics framework developed by Munafò et al. [21], capable of simulating inductively-coupled plasma flows. Using the approach and computational domain specified in our previous work [22], simulations were performed in air plasma for the 40 mm iso-Q sample geometry for the four test conditions, assuming non-local thermodynamic equilibrium. For the simulations, the delivered torch power, mass flow rate, and chamber pressure were specified based on experimental operating conditions in Table 2 of the main paper. An isothermal boundary condition was imposed at the stagnation surface of the sample with a fixed hot-wall temperature based on pyrometer measurements. On the side surface of the samples, a similar isothermal boundary condition with a temperature of 1473 K was imposed. From the simulations, pressure profiles along the sample surface were extracted and used for the Thiele number analysis. Further details on the simulation framework, computational domain, and boundary conditions are reported in [22].

References

[1] D. Lanza, M. Franco, G. Elliott, M. Panesi, F. Panerai, Plasflowsolver: An aerothermodynamic data reduction model for inductively coupled plasma wind tunnel facilities, in: AIAA SCITECH 2025 Forum, 2025, p. 0449.

[2] T. Oldham, L. Capponi, M. Konnik, K. Stephani, D. J. Bodony, M. Panesi, G. S. Elliott, F. Panerai, Aerothermal characterization of the plasmatron x wind tunnel: optical emission spectroscopy and jet temperature reconstruction, in: AIAA Scitech 2023 Forum, 2023, p. 2516.

[3] M. Winter, B. Butler, P. M. Danehy, S. Splinter, Z. Diao, F. Panerai, A. Martin, S. Bailey, Characterization of ablation product radiation signatures of pica and fiberform, in: 46th AIAA Thermophysics Conference, 2016, p. 3233.

[4] T. Czerwiec, F. Greer, D. Graves, Nitrogen dissociation in a low pressure cylindrical icp discharge studied by actinometry and mass spectrometry, Journal of Physics D: Applied Physics 38 (24) (2005) 4278.

[5] B. Helber, A. Turchi, T. E. Magin, Determination of active nitridation reaction efficiency of graphite in inductively coupled plasma flows, Carbon 125 (2017) 582–594.

[6] F. Panerai, A. Martin, N. N. Mansour, S. A. Sepka, J. Lachaud, Flow-tube oxidation experiments on the carbon preform of a phenolic-impregnated carbon ablator, Journal of Thermophysics and Heat Transfer 28 (2) (2014) 181–190.

[7] J. Lachaud, N. Mansour, A. Ceballos, D. Pejakovic, L. Zhang, J. Marschall, Validation of a volume-averaged fiber-scale model for the oxidation of a carbon-fiber preform, in: 42nd AIAA Thermophysics Conference, 2011, p. 3640.

[8] B. Helber, A. Turchi, J. B. Scoggins, A. Hubin, T. E. Magin, Experimental investigation of ablation and pyrolysis processes of carbon-phenolic ablators in atmospheric entry plasmas, International Journal of Heat and Mass Transfer 100 (2016) 810–824.

[9] C. W. Foster, Micro-to-meso scale high temperature response of ablative systems for atmospheric entry, Ph.D. thesis, University of Illinois Urbana-Champaign (2024).

[10] B. Helber, C. O. Asma, Y. Babou, A. Hubin, O. Chazot, T. E. Magin, Material response characterization of a low-density carbon composite ablator in high-enthalpy plasma flows, Journal of materials science 49 (2014) 4530–4543.

[11] B. K. Bessire, T. K. Minton, Decomposition of phenolic impregnated carbon ablator (pica) as a function of temperature and heating rate, ACS Applied Materials & Interfaces 9 (25) (2017) 21422–21437.

[12] F. S. Milos, Y.-K. Chen, Ablation and thermal response property model validation for phenolic impregnated carbon ablator, Journal of Spacecraft and Rockets 47 (5) (2010) 786–805.

[13] B. M. Ringel, H. J. Boesch, S. Oruganti, L. Villafañe Roca, F. Panerai, Unsteady spallation of low-density carbon fiber ablators, Carbon (2025).

[14] C. H. Guiles, Y. Benitez, G. N. Morales, J. D. Engerer, B. A. Hernandez-Sanchez, T. K. Minton, Pyrolysis of phenolic resin investigated by molecular beam mass spectrometry, ACS Applied Materials & Interfaces (2025).

[15] E. W. Thiele, Relation between catalytic activity and size of particle, Industrial & Engineering Chemistry 31 (7) (1939) 916–920.

[16] B. M. Ringel, F. Semeraro, J. C. Ferguson, H. S. Barnard, B. Dias, C. M. Schlepütz, E. S. Barnard, S. Schickler, K. Levy, S. Shacterman, et al., Carbon fiber oxidation in 4d, Advanced Materials (2025) 2502007`doi:10.1002/adma.202502007`.

[17] N. A. Anderson, P. Zolfaghari, S. Bhattacharya, L. Capponi, T. Oldham, R. M. Sankaran, G. S. Elliott, F. Panerai, Flow reactor experiments of high-temperature graphite oxidation and nitridation, High Temperature Corrosion of Materials (2024) 1–17.

[18] J. Lachaud, I. Cozmuta, N. N. Mansour, Multiscale approach to ablation modeling of phenolic impregnated carbon ablators, Journal of Spacecraft and Rockets 47 (6) (2010) 910–921. `doi:10.2514/1.42681`.

[19] J. B. Scoggins, V. Leroy, G. Bellas-Chatzigeorgis, B. Dias, T. E. Magin, Mutation++: Multicomponent thermodynamic and transport properties for ionized gases in c++, SoftwareX 12 (2020) 100575.

[20] W. Pollard, R. D. Present, On gaseous self-diffusion in long capillary tubes, Physical Review 73 (7) (1948) 762.

[21] A. Munafò, R. Chiodi, S. Kumar, V. Le Maout, K. A. Stephani, F. Panerai, D. J. Bodony, M. Panesi, A multi-physics modeling framework for inductively coupled plasma wind tunnels, in: AIAA SCITECH 2022 Forum, 2022, p. 1011.

[22] S. Oruganti, S. Kumar, V. Le Maout, L. Capponi, A. Munafo, D. J. Bodony, M. Panesi, F. Panerai, N. Mansour, S. Fraile Izquierdo, Modeling instrumented test articles for plasmatron x aerothermal environment, in: AIAA Aviation 2023 Forum, 2023, p. 3327.